

1 **Effect of AMOC collapse on ENSO in a high**  
2 **resolution general circulation model**

3 **Mark S. Williamson · Mat Collins ·**  
4 **Sybren S. Drijfhout · Ron Kahana ·**  
5 **Jennifer V. Mecking · Timothy M. Lenton**

6  
7 Received: date / Accepted: date

8 **Abstract** We look at changes in the El Niño Southern Oscillation (ENSO) in  
9 a high-resolution eddy-permitting climate model experiment in which the At-  
10 lantic Meridional Circulation (AMOC) is switched off using freshwater hosing.  
11 The ENSO mode is shifted eastward and its period becomes longer and more reg-  
12 ular when the AMOC is off. The eastward shift can be attributed to an anomalous  
13 eastern Ekman transport in the mean equatorial Pacific ocean state. Convergence  
14 of this transport deepens the thermocline in the eastern tropical Pacific and in-  
15 creases the temperature anomaly relaxation time, causing increased ENSO period.  
16 The anomalous Ekman transport is caused by a surface northerly wind anomaly  
17 in response to the meridional sea surface temperature dipole that results from  
18 switching the AMOC off. In contrast to a previous study with an earlier version  
19 of the model, which showed an increase in ENSO amplitude in an AMOC off ex-  
20 periment, here the amplitude remains the same as in the AMOC on control state.  
21 We attribute this difference to variations in the response of decreased stochastic  
22 forcing in the different models, which competes with the reduced damping of tem-

---

Mark S. Williamson  
Earth System Science group, College of Life and Environmental Sciences, University of Exeter,  
Laver Building, North Park Road, Exeter EX4 4QE, UK.  
E-mail: m.s.williamson@exeter.ac.uk

Mat Collins  
College of Engineering, Mathematics and Physical Sciences, University of Exeter, Exeter, UK.

Sybren S. Drijfhout  
Ocean and Earth Science, National Oceanography Centre Southampton, University of  
Southampton, SO14 3ZH, UK.

Ron Kahana  
Hadley Centre, Met Office, Exeter, UK.

Jennifer V. Mecking  
Ocean and Earth Science, National Oceanography Centre Southampton, University of  
Southampton, SO14 3ZH, UK.

Timothy M. Lenton  
Earth System Science group, College of Life and Environmental Sciences, University of Exeter,  
Laver Building, North Park Road, Exeter EX4 4QE, UK.

23 perature anomalies. In the new high-resolution model, these effects approximately  
24 cancel resulting in no change in amplitude.

## 25 1 Introduction

26 The net transport of heat from the equator to higher northern latitudes in the  
27 Atlantic caused by the flow of upper water layers in the Atlantic ocean, part of  
28 the Atlantic meridional overturning circulation (AMOC), is responsible for the  
29 mild winters in western Europe. This net ocean flow is part of a larger ocean  
30 mode known as the thermohaline circulation. Simple models of this circulation  
31 show tipping point like behaviour i.e. they can abruptly switch from one mode  
32 to another when changes in climatic conditions are comparatively small and slow  
33 (Stommel 1961; Rooth 1982; Marotzke and Willebrand 1991). It has been shown  
34 that the Atlantic branch of this circulation can abruptly switch off under certain  
35 conditions causing major changes in the climate not only in the North Atlantic but  
36 also globally (Vellinga and Wood 2002; Stouffer et al 2006; Jackson et al 2015). It  
37 is thought that this has happened in the past Earth history (Dansgaard-Oeschger  
38 events and Heinrich stadials (Rahmstorf 2002; Clement and Peterson 2006)) and  
39 although present research suggests a collapse of the Atlantic MOC is unlikely to  
40 occur in the 21st century under global warming scenarios (Collins et al 2013), the  
41 impacts of a shutdown are severe making it a low probability high impact event.  
42 Even though a shutdown is thought to be unlikely by the end of the 21st century,  
43 a weakening in AMOC was assessed to be very likely by the IPCC AR5 (Collins  
44 et al 2013) making assessment of the impacts of this tipping point, both regional  
45 and global, a useful exercise.

46 In future climate model projections, emissions are prescribed causing a reduc-  
47 tion or perhaps a shutdown of the AMOC indirectly along with other climate  
48 impacts. The work reported here differs in that only the impacts of AMOC shut-  
49 down are assessed. This is done by forcing a high resolution Earth system model  
50 into a collapsed AMOC state directly using a large salinity perturbation applied  
51 for 10 years, without changing anything else (such as emissions). The AMOC off  
52 state in this simulation is stable over the 450 years duration of the model inte-  
53 gration (Mecking et al 2016) which is then compared with a control run making  
54 the study a comparatively clean assessment of the impacts of AMOC shutdown.  
55 The model used is a state of the art global climate model (HadGEM3), a high  
56 resolution general circulation model with coupled ocean, atmosphere, sea ice and  
57 land surface and hydrology.

58 Similar ‘freshwater hosing’ experiments have been performed with models of  
59 differing complexity, from other coupled GCMs (Vellinga and Wood 2002) to mod-  
60 els of intermediate complexity (Rahmstorf et al 2005). In these studies, removing  
61 such a large ocean flux of heat into the North Atlantic causes a large reorganization  
62 of the global climate, amongst these impacts there is substantial cooling around  
63 the North Atlantic region and a southward shift in the intertropical convergence  
64 zone (ITCZ).

65 We look in particular at the differences in ENSO resulting from the global  
66 climatic changes that collapse of the AMOC can induce in the model. ENSO is  
67 a coupled ocean-atmosphere oscillatory mode in the equatorial Pacific and the  
68 dominant global mode of natural unforced variability. Its effects are large enough

69 to change the typical global climate patterns. ENSO oscillates between two states,  
70 a warm state, El Niño, and a cold state, La Niña, with a period of around 3 to 7  
71 years. Typically the western side of the equatorial Pacific has some of the highest  
72 sea surface temperatures (SSTs) on the planet. This ‘warm pool’ causes a net wind  
73 to blow east to west pushing surface waters westward and causing a depression in  
74 the western Pacific thermocline and a lifting of the thermocline in the east. This  
75 lifting in the east causes cold, nutrient rich deep waters to upwell off the South  
76 American coast. Every few years this quasi-steady phase breaks down, the net  
77 wind ceases, the thermocline adjusts to the new pressure gradient and the warm  
78 pool propagates west to east across the Pacific in an El Niño event causing the  
79 SSTs in the the east to rise and the thermocline to deepen inhibiting the cold  
80 waters from upwelling. This is a large scale energy readjustment on the global  
81 scale and changes typical weather patterns significantly.

82 Making concrete statements on ENSO behaviour has proved difficult due to the  
83 delicate balance of ocean and atmosphere feedbacks that determine its character-  
84 istics (Collins et al 2010). In modelling studies, decadal or centennial modulations  
85 can be generated without any change in external forcing (Wittenberg 2009). In-  
86 cluding changing forcing and changing mean conditions makes attributing changes  
87 even more difficult. Because of this sensitive balance different models forced with  
88 the same boundary conditions have produced a wide range of ENSO behaviours  
89 (Bellenger et al 2014).

90 There have also been studies of ENSO in hosed, weakened AMOC runs of  
91 CMIP3 era models (Timmerman et al 2007; Dong and Sutton 2007) and in most  
92 models there was a substantial weakening of the annual cycle in the eastern equa-  
93 torial Pacific and an increase in ENSO amplitude. Both of these traits were found  
94 in HadCM3 (an earlier generation of the Met Office Hadley Centre model) as  
95 well as an eastern shift in the ENSO mode (Dong and Sutton 2007). We find the  
96 same eastern shift and weakened annual cycle in HadGEM3 however they differ  
97 in ENSO period response, going to longer periods in HadGEM3 (there was no sig-  
98 nificant change in HadCM3) and the amplitude remains approximately the same  
99 (HadCM3 ENSO amplitude increased by about a third).

100 Using a stochastically forced damped oscillator model of slow ENSO dynamics  
101 introduced by Jin (1997) to qualitatively understand the response of the much  
102 more complicated HadGEM3, we suggest the difference in ENSO amplitude be-  
103 tween the different models is due to the balance of changes in ENSO damping and  
104 the magnitude of stochastic forcing. To be more concrete, reduced damping in this  
105 model means larger amplitude ENSO oscillations for a fixed forcing magnitude.  
106 In the AMOC off run this reduced damping is caused by the increased eastern  
107 Pacific temperature anomaly relaxation times from the deeper thermocline. Thus  
108 higher ENSO amplitudes should result. However, the decreased stochastic forcing  
109 of the oscillations offsets this increase. The overall ENSO amplitude is therefore a  
110 competition between these two competing effects.

111 In section 2 we describe the model and experiment design. In section 3 we  
112 briefly describe the model states in both AMOC off and control runs before ana-  
113 lyzing the dominant tropical Pacific modes of variability, their amplitudes, power  
114 spectra and autocorrelation functions and differences between the simulations. In  
115 section 4 we provide mechanisms and the supporting evidence for the differences  
116 between the ENSOs in both simulations and discuss these results in the context  
117 of previous findings in section 5. Conclusions are given in section 6.

## 118 2 Model setup and experiment design

### 119 2.1 Model description

120 The model and its performance has previously been described in detail elsewhere  
121 (Williams et al 2015). To repeat pertinent details, the model is the Global Coupled  
122 2.0 model (GC2) configuration of the HadGEM3 model (Hewitt et al 2011). This  
123 consists of an atmosphere, ocean, sea-ice and land-surface models. The atmosphere  
124 model is Global Atmosphere vn6.0 (GA6) (Demory et al 2013) of the Met Office  
125 unified model at N216 horizontal resolution and 85 levels in the vertical. The ocean  
126 model is the Global Ocean 5 (GO5) (Megann et al 2013) version of the ORCA025  
127 configuration of the NEMO model (Madec 2008) with a eddy permitting horizontal  
128 resolution of  $0.25^\circ$  and 75 vertical levels. The sea-ice model is version 4.1 of the  
129 Los Alamos National Laboratory sea-ice model, CICE (Hunke and Lipscomb 2010)  
130 and resolution is the same as that of the ocean model. The land model used in GC2  
131 is the GL6 configuration of the Joint UK Land Environment Simulator (JULES).  
132 The model simulates the state of the soil and 5 vegetation types (broadleaf trees,  
133 needleleaf trees, C3 (temperate) grass, C4 (tropical) grass, and shrubs) in each land  
134 grid box. The distribution of these plant types is fixed throughout the simulations.

#### 135 2.1.1 Experiment design

136 Details of the experimental design and of the runs we analyze here have also been  
137 given previously (Jackson et al 2015; Mecking et al 2016). Two runs of the model  
138 are compared, a steady state control run (the AMOC is in its usual on state in  
139 this run) and an AMOC off steady state run. To do this the model was initialised  
140 from climatology and spun up for over 36 years. The control run is then integrated  
141 for a further 150 years. To collapse the AMOC the methodology of Vellinga and  
142 Wood (2002) is used which involves perturbing the salinity in the upper layers of  
143 the North Atlantic to inhibit deep convection and hence quickly shut down the  
144 AMOC. (The absence of the sinking branch of the AMOC is what we will refer to as  
145 the AMOC off state.) Although this method of collapsing the AMOC is unrealistic  
146 (freshwater addition from melt of the Greenland ice sheet and Arctic runoff are the  
147 most likely cause of AMOC shutdown in global warming projections) it is useful  
148 for investigating the impacts of a shutdown. The AMOC off run is initialised after  
149 42 years of the control run. Instantaneous salinity perturbations are applied to  
150 the upper 536 m of the Atlantic and Arctic Ocean north of  $20^\circ\text{N}$  each December  
151 for the first 10 years at which point hosing ceases. Each salinity perturbation is  
152 equivalent to continuously adding freshwater at a rate of 1 Sv ( $1\text{ Sv}=10^6\text{ m}^3\text{s}^{-1}$ )  
153 for 10 years (total of 10 SvYr). As is common practice in hosing experiments the  
154 salinity in the rest of the ocean is also perturbed such that the total freshwater  
155 content of the global ocean remains constant. The AMOC off run is integrated for  
156 a total of 450 years from the start of the salinity perturbations. No external forcing  
157 is applied to the model apart from diurnal and annual cycles of the radiative fluxes.  
158 Atmospheric  $\text{CO}_2$  concentrations are fixed to 1978 levels.

159 As the perturbations are applied, the AMOC collapses from the steady  $\sim 15\text{ Sv}$   
160 (maximum streamfunction at  $26.5^\circ\text{N}$ ) in the control run and remains very weak  
161 for the full model simulation period of 450 yrs. As a result meridional Atlantic  
162 ocean heat transport at  $30^\circ\text{N}$  is halved from  $\sim 1\text{ PW}$  to  $\sim 0.5\text{ PW}$  and surface

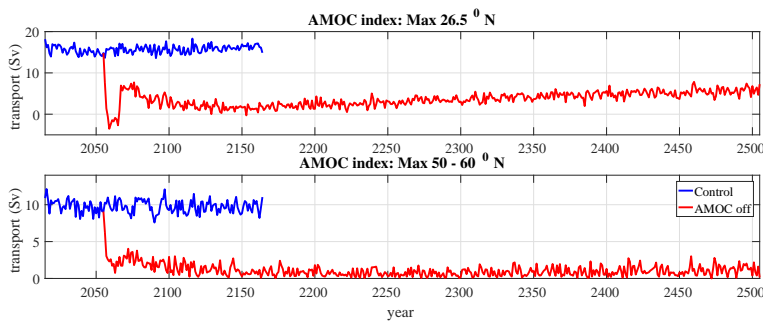


**Fig. 1** Maximum in the AMOC streamfunction at  $26.5^{\circ}\text{N}$  and  $50 - 65^{\circ}\text{N}$  between depths of 500 - 2000 m. Blue line is the control, red line is the AMOC off run. Hosing is applied for 10 years at the beginning of the AMOC off run resulting in a relatively stable off state for the remaining duration of the simulation. The last 300 years of the AMOC off run and the full 150 yrs of the control run are analyzed in the rest of the manuscript.

163 air temperature (SAT) is reduced by  $\sim 4^{\circ}\text{C}$  in the North Atlantic (Jackson et al  
 164 2015). The AMOC off simulation is approximately stationary 60 years after the  
 165 salinity perturbations end however the maximum in the AMOC streamfunction  
 166 at  $26.5^{\circ}\text{N}$  does have a very slow increasing trend reaching  $\sim 5\text{ Sv}$  at the end of  
 167 the 450 years. Further north however, the AMOC shows no signs of recovering  
 168 (Mecking et al (2016), see figure 1).

169 In the following analysis we use all 150 years of the control run and the last  
 170 300 years of the AMOC off run to determine ENSO properties.

### 171 3 Results

#### 172 3.1 Climate in the HadGEM3 control run

173 General information on the climate states of the control (Williams et al 2015) and  
 174 AMOC off runs have been given previously in Jackson et al (2015) and Mecking  
 175 et al (2016) and we give brief details here.

176 One of the robust feature of hosing simulations is the widespread cooling particu-  
 177 larly in the North Atlantic and northern hemisphere in general (Stouffer et al  
 178 (2006); Vellinga and Wood (2002), figure 2). This is accompanied by a slight warm-  
 179 ing in the southern hemisphere to give the well known anomalous cool northern  
 180 hemisphere-warm southern hemisphere dipole, southward shift in the intertropi-  
 181 cal convergence zone (ITCZ) and associated changes in equatorial precipitation  
 182 patterns as a new energy balance between the hemispheres is reached. The north  
 183 Atlantic cooling results in more Arctic sea-ice and intensification of storm tracks  
 184 (Jackson et al 2015). Globally, the annual mean SAT is lower when the AMOC is  
 185 off ( $15.1^{\circ}\text{C}$  compared to  $16.2^{\circ}\text{C}$  in the control run). Variability in global annual  
 186 mean SAT is increased in the AMOC off run (standard deviations of  $1.52^{\circ}\text{C}$  in the  
 187 AMOC off and  $1.33^{\circ}\text{C}$  in the control) although the reverse is true in the annual  
 188 mean taken over the tropical Pacific region (standard deviations of  $0.52^{\circ}\text{C}$  in the  
 189 AMOC off and  $0.67^{\circ}\text{C}$  in the control). One of the unique features of the HadGEM3  
 190 simulations is the stability of the AMOC off state. Usually the AMOC off state  
 191 recovers when freshwater hosing is removed. Here it remains stable. Mecking et al

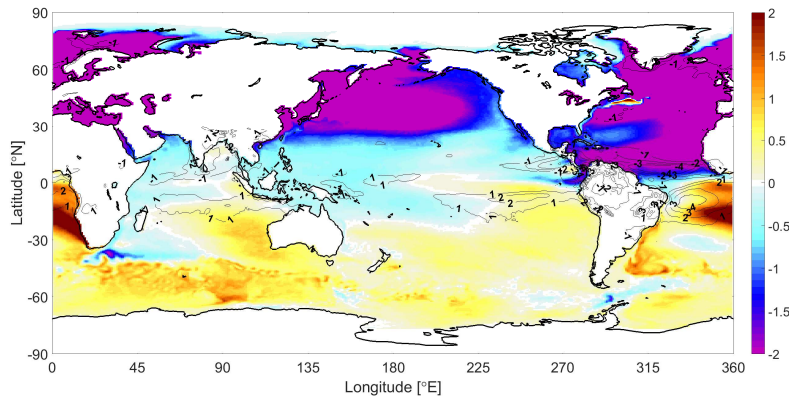


**Fig. 2** Global patterns of the annual mean sea surface temperature (SST) anomaly (AMOC off - control) in the colour plot. The scale is in  $^{\circ}\text{C}$ . There is a widespread cooling particularly in the North Atlantic and northern hemisphere in general. This is accompanied by a slight warming in the southern hemisphere to give the well known anomalous cool northern hemisphere-warm southern hemisphere dipole when the AMOC is off. The black contour lines are the annual mean precipitation anomaly in mm/day. Generally, when the AMOC is off the northern hemisphere becomes drier and the southern hemisphere becomes wetter. The ITCZ is also shifted southward.

192 (2016) report that this is due to the eddy permitting ocean model allowing for a  
 193 stronger northward freshwater transport.

194 HadGEM3 in GC2 configuration was shown to be an improvement over pre-  
 195 vious versions of the Met Office Hadley Centre model particularly in the modes  
 196 of variability such as mid-latitude and tropical cyclone intensities, the Madden-  
 197 Julian Oscillation (MJO) and ENSO (Williams et al 2015). Excess equatorial  
 198 easterly wind stress has been a problem in previous versions of Met Office mod-  
 199 els. A number of changes have made this better including the improvement of  
 200 MJO simulation, although its amplitude remains significantly weaker than ob-  
 201 served, which can be a source of westerly wind bursts that initiate El Niño events.  
 202 Higher horizontal ocean resolution has also improved ENSO simulation (good spa-  
 203 tial pattern, SST variability). ENSO period also falls in to the observed range of  
 204 3-7 years with no dominant 2 year or longer period peaks in the power spec-  
 205 trum that have been a problem in older coupled GCMs (Bellenger et al 2014).  
 206 Overall the model compares well with a range of CMIP5 models (Bellenger et al  
 207 2014) and historical observations. The control run however slightly underestimates  
 208 SST variability, more so in the western tropical Pacific and the distribution of  
 209 SST anomalies is slightly skewed towards cold events whereas in observations a  
 210 warm skew is more typically present. SST statistics in the control run and histor-  
 211 ical observations (1870 - 2015) are given in table 1 although it should be noted  
 212 the comparison is not completely equivalent as there are no changes in forcing  
 213 in the control run. Historical observations were taken from the NOAA website  
 214 [http://www.esrl.noaa.gov/psd/gcos\\_wgsp/Timeseries/Plot/index.htm](http://www.esrl.noaa.gov/psd/gcos_wgsp/Timeseries/Plot/index.htm).

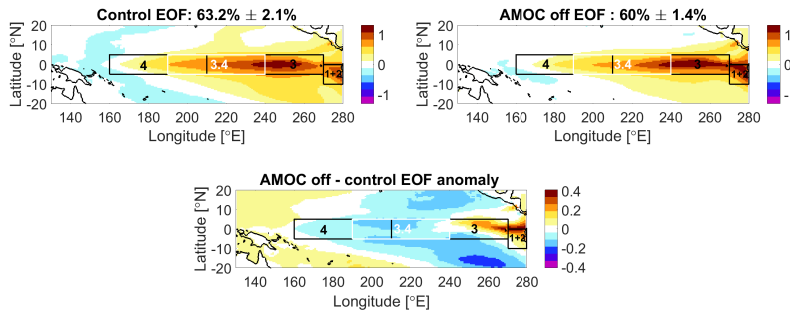


**Fig. 3** The largest mode of variability (EOF) representative of ENSO in the deseasonalized monthly SST fields in the control (upper left) and AMOC off simulations (upper right). The proportion of the variance the mode accounts for within each run is shown as a percentage in the title above each plot with estimated error (North et al 1995). The lower row shows the anomaly between the runs. The EOF is shifted eastward in the AMOC off run. Units are  $^{\circ}\text{C}$ . Niño regions are indicated by the boxes. Moving east to west these are Niño 1+2, Niño 3, Niño 3.4 (white box) and Niño 4. Most of the ENSO variability in the model is captured in Niño 3.

### 215 3.2 Dominant modes of variability in the tropical Pacific

216 To determine the spatial modes of maximal variability we calculate the leading  
 217 empirical orthogonal function (EOF) (the eigenvector of the covariance matrix  
 218 associated to the largest eigenvalue) from monthly fields of sea surface temperature  
 219 (SST). The monthly spatial SST fields are taken over the tropical Pacific region  
 220 bounded by the box  $\pm 20^{\circ}\text{N}$  and  $130^{\circ}\text{E}$  and  $280^{\circ}\text{E}$  which are deseasonalized by  
 221 subtracting the long term monthly mean at each grid point. We calculate the  
 222 covariance matrix for the full duration (150 years) of the control run and the  
 223 last 300 years of the AMOC off run. The leading EOF and the proportion of  
 224 the variance it accounts for within each run is shown in figure 3. The second EOF  
 225 associated to the Modoki mode (not shown) (Ashok and Yamagata 2009), accounts  
 226 for about 15 % of the variance in both runs.

227 The leading EOF in both the control and the AMOC off run is representa-  
 228 tive of the ENSO mode. Relative to the control run, the AMOC off ENSO EOF  
 229 accounts for proportionally slightly less of the total variance in SST (60% versus  
 230 63%) although this difference, both proportional and absolute, is within estimated  
 231 error bounds. The spatial pattern however is shifted eastward and is slightly more  
 232 equatorially confined as can be seen in the anomaly. We have tested that this spa-  
 233 tial shift is significant at the 99% level. More specifically, the variance differences  
 234 at each spatial location were tested for significance at the 99% confidence level by  
 235 performing a two sample f-test on the deseasonalized spatial SST anomaly fields in  
 236 both control and AMOC off runs. Most of the variability in both runs is contained  
 237 in the Niño 3 region.

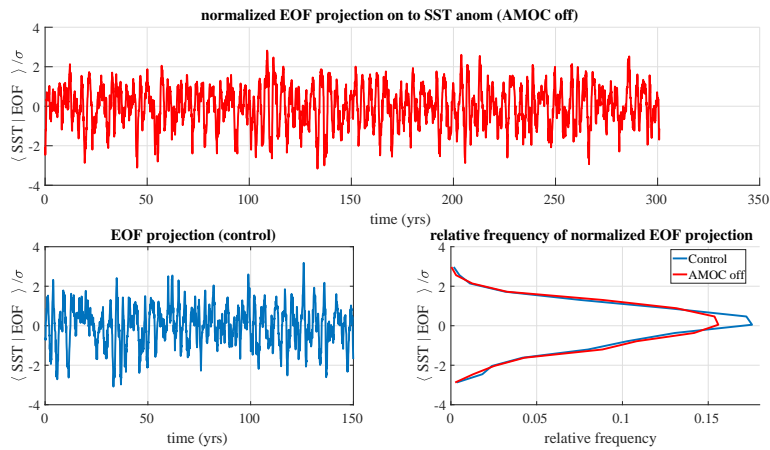


**Fig. 4** Projection of the leading EOF in figure 3 on to the timeseries of the SST anomaly fields normalized by the standard deviation of the projection time series (AMOC off projection in the upper panel, control projection in the lower left panel). The lower right panel is the relative frequency of these values. The blue line is the control run and the red is the AMOC off run.

### 238 3.3 ENSO amplitude and distribution

239 We next look at the time series and amplitude distribution of the leading mode of  
 240 SST variability as well as the distributions of the more traditional Niño 1+2, 3,  
 241 3.4 and 4 indices. Time varying properties are analyzed by projecting the leading  
 242 EOF onto the time ordered fields of deseasonalized monthly SST for both control  
 243 and AMOC off runs. This produces a time series of how strong the spatial mode is  
 244 at each point in time throughout the run and is much like a Niño index although  
 245 it is more specific in that it captures the time varying properties of just this mode.  
 246 The time series of the EOF projection are given in figure 4 (upper and lower left  
 247 panel). The projection in the AMOC off run has some drift probably due to the  
 248 long time taken for the deep ocean to re-equilibrate with the new AMOC off ocean  
 249 mode. This drift is removed by linearly detrending the AMOC off EOF projection  
 250 for calculation of the periodogram and autocorrelation functions in section 3.4.  
 251 This is to remove any spurious low frequency/long time scale correlations that a  
 252 linear trend can introduce.

253 We have plotted the frequency of the value in the detrended EOF time series  
 254 projection in figure 4 (lower right panel). We have also plotted the frequency  
 255 of deseasonalized SST anomalies in each of the Niño regions as a more traditional  
 256 comparison with the leading EOF mode (figure 5). These values are the mean SST  
 257 anomalies over the regions, going from tropical east Pacific to west shown in figure  
 258 3, Niño 1+2 (equatorial South American Pacific coast, bounded by the box 0-10°S,  
 259 270 - 280°E), Niño 3 (eastern tropical Pacific, 5°S - 5°N, 210 - 270° E), Niño 3.4  
 260 (central tropical Pacific, 5°S - 5°N, 190 - 240° E) and Niño 4 (western tropical  
 261 Pacific, 5°S - 5°N, 160 - 210° E). In general distributions become narrower (less  
 262 variability) and more skewed towards cold events the further west one goes. Both  
 263 runs have very similar amplitudes, standard deviations and skewness although

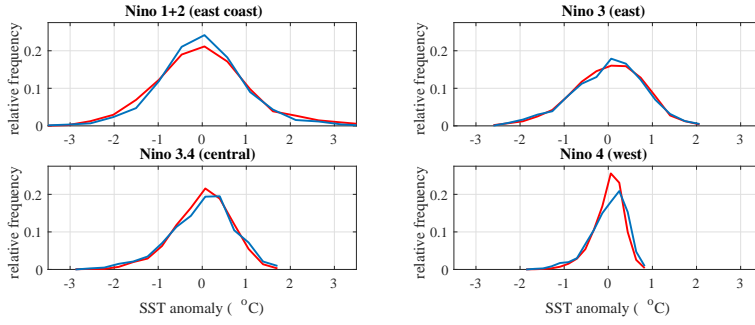


**Fig. 5** Histograms of the deseasonalized SST anomalies in each of the Niño regions. Niño 1+2 is situated just off the equatorial South American coast, Niño 3 is eastern equatorial Pacific, Niño 3.4 is central equatorial Pacific and Niño 4 is western equatorial Pacific. Blue lines are the control run and red lines are the AMOC off run. In general distributions become narrower (less variability) and more skewed towards cold events the further west one goes. This is also seen in observations (table 1). Both runs have very similar amplitudes, standard deviations and skewness.

**Table 1** Mean, standard deviation and skewness of the deseasonalized leading SST EOF and the same for the Niño regions in the control run, AMOC off run and historical observations. In general SSTs are skewed more towards colder events and the amplitude (given roughly by the standard deviation) decreases the further west one goes in both the models and observations. Apart from the eastern shift in the AMOC off run both model runs are very similar. Historical observations compare favorably with the control run although the observations tend to have more variability in the western Pacific and a positive (warm event skew), rather than negative (cold event) skew. Historic observation data is taken from the NOAA website.

	Observations	Control	AMOC off
mean Niño 1+2 SST	23.23 °C	25.45 °C	25.48 °C
mean Niño 3 SST	25.74 °C	26.70 °C	26.73 °C
mean Niño 3.4 SST	26.96 °C	27.68 °C	27.69 °C
mean Niño 4 SST	28.37 °C	28.93 °C	28.85 °C
Niño 1+2 std (monthly mean removed)	2.25 (0.91) °C	2.21 (0.96) °C	2.31 (1.07) °C
Niño 3 std (monthly mean removed)	1.19 (0.80) °C	1.13 (0.81) °C	0.96 (0.80) °C
Niño 3.4 std (monthly mean removed)	0.89 (0.77) °C	0.77 (0.73) °C	0.69 (0.65) °C
Niño 4 std (monthly mean removed)	0.60 (0.57) °C	0.52 (0.42) °C	0.52 (0.35) °C
Niño 1+2 skew (monthly mean removed)	0.19 (1.13) °C <sup>3</sup>	-0.04 (0.16) °C <sup>3</sup>	-0.23 (0.33) °C <sup>3</sup>
Niño 3 skew (monthly mean removed)	0.14 (0.76) °C <sup>3</sup>	-0.23 (-0.30) °C <sup>3</sup>	-0.23 (-0.31) °C <sup>3</sup>
Niño 3.4 skew (monthly mean removed)	-0.04 (0.41) °C <sup>3</sup>	-0.51 (-0.46) °C <sup>3</sup>	-0.51 (-0.46) °C <sup>3</sup>
Niño 4 skew (monthly mean removed)	-0.23 (-0.10) °C <sup>3</sup>	-0.53 (-0.88) °C <sup>3</sup>	-0.44 (-0.91) °C <sup>3</sup>
EOF std	N/A	41.70 °C	39.02 °C
EOF skew	N/A	-0.26 °C <sup>3</sup>	-0.23 °C <sup>3</sup>

264 one can see a shift eastward in the Niño indices for the AMOC off runs which  
 265 was also picked up by the spatial anomaly in the EOF. We have tabled the values  
 266 of mean, standard deviation and skewness for the EOF projection and the Niño  
 267 indices in table 1. Amplitudes in the SST anomalies (seasonal mean removed)  
 268 given approximately by the standard deviation are very similar although slightly  
 269 lower in the AMOC off run.

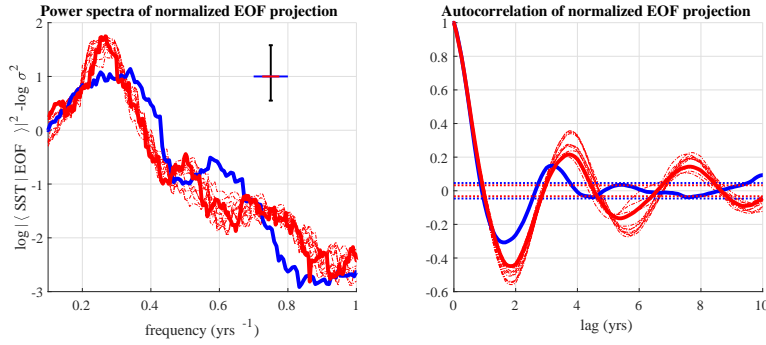


**Fig. 6** Power spectra (left panel) of the linearly detrended normalized EOF timeseries in figure 4 and the autocorrelation functions (right panel). The thick blue lines are the control run and the thick red is the spectrum of all 300 years of the AMOC off run. The thin red lines are eleven 150 year segments of the AMOC off run spaced 15 years apart. The spectra are estimated by smoothing the raw periodograms (Daniell spectral estimator) with a rectangular window of 15 points (bandwidth of control run is  $\Delta f = 15/150 = 0.1$  cycles/yr and  $\Delta = 15/300 = 0.05$  cycles/yr for the AMOC off run and is plotted as the horizontal error bar). The vertical error bar is the 95% confidence interval. In the autocorrelation function plots dotted lines represent the 95% confidence interval of the null hypothesis. The EOF has clear periodicities, the AMOC off run being shifted to longer periodicities of just under 4 years compared of the control run which is closer to 3 years.

### 270 3.4 Spectra and autocorrelation of EOF projection

271 In figure 6 (left panel) we calculate the smoothed periodogram of the linearly detrended  
 272 EOF projection time series with 95% confidence intervals and bandwidths  
 273 given by the error bar. In the control run (thick blue line) the leading EOF has a  
 274 broad spectral peak of width  $\sim 0.1$  cycles/yr (approximately the bandwidth resolu-  
 275 tion) with a maximum at 0.34 cycles/yr (a period of 2.9 yrs). The periodogram  
 276 of the AMOC off run (thick red line) has a much sharper peak of width  $\sim 0.05$   
 277 cycles/yr (again, approximately the bandwidth) and maximum 0.26 cycles/yr cor-  
 278 responding to a period of 3.9 yrs. The sharper peak in the AMOC off run may be  
 279 due to the longer time series giving a better estimate of the mean ENSO frequency.  
 280 We have tested this by cutting the AMOC off time series to the same length as the  
 281 control run (150 yrs) and computing the smoothed periodograms for 11 segments  
 282 spaced 15 years apart (thin red lines). Peaks do get wider as expected however they  
 283 were still narrower than the control run suggesting a more regular, less damped  
 284 oscillation. There is also a shift to longer ENSO periods in the AMOC off relative  
 285 to the control run which does appear to be significantly different.

286 An alternative way to look at the same information provided by the peri-  
 287 odogram is the autocorrelation function of a time series, the difference being the  
 288 information is presented in the time rather than the frequency domain. Autocor-  
 289 relation functions are presented in the right panel of figure 6. The thick blue line is  
 290 the control run and thick red line is the full 300 years of the AMOC off run. Thin  
 291 red lines are the eleven 150 year segments of the AMOC off run spaced 15 years  
 292 apart. Dotted lines represent the 95% confidence interval for the null hypothesis.  
 293 The autocorrelation has a clear, damped oscillatory character. This is particu-  
 294 larly prominent in the AMOC off run with multiple cycles of period 45 months  
 295 having greater correlation than the 95% confidence bound of the null hypothesis.

296 This supports the sharper, more regular, ENSO thought to be present from peri-  
297 odogram analysis. In contrast the control run had a broader peak centered around  
298 a 38 month period. The oscillation in the autocorrelation function is washed out  
299 below the confidence interval after just one cycle in the control run suggesting that  
300 the ENSO period is more heavily damped in the control run.

## 301 4 Mechanisms for differences in ENSO

302 Having established that ENSO in the AMOC off run relative to the control has  
303 (i) a similar amplitude and distribution of SST anomalies, (ii) a spatial pattern  
304 shifted eastward and (iii) a longer, more regular period, we discuss mechanisms  
305 that could result in these differences.

### 306 4.1 Eastward shift in ENSO

307 The eastward shift in the ENSO mode in the AMOC off run is also accompanied  
308 by an eastward shift in the mean equatorial Pacific state. It seems likely therefore  
309 that the shift in SST variability results from the mode being shifted eastward with  
310 the mean state. We propose a mechanism for the shift in the mean state and then  
311 show the patterns in variability are also shifted east.

#### 312 4.1.1 Eastward shift in mean state

313 An executive summary of basic mechanism of the shift in the Pacific mean state  
314 is as follows (we go into more detail in the following paragraphs): The anomalous  
315 north-south temperature dipole (figure 2) causes a north to south surface wind  
316 anomaly associated to the southward shift of the ITCZ (figure 8, lower right panel,  
317 dotted lines) as the higher pressure, cooler air in the northern hemisphere flows  
318 towards the rising lower pressure, warmer air in the southern hemisphere. This  
319 anomalous north to south surface wind exerts an anomalous north to south wind  
320 stress on the surface of the ocean and results in wind driven (Ekman) transport in  
321 the upper ocean waters. The transport is to the right of the wind stress vector in  
322 the northern hemisphere and to the left in the south. It is the anomalous eastern  
323 Ekman transport in the southern hemisphere (figure 9) that results in the eastward  
324 shift as a new east-west dynamic balance is reached.

325 Supporting evidence for this mechanism is presented next: In figure 7 SST  
326 fields in the equatorial Pacific for both runs and their difference are given. Note  
327 that the Pacific cold tongue is slightly warmer in the AMOC off run. In the bottom  
328 right hand corner we have plotted the annual mean SST integrated between  $5^{\circ}\text{S}$   
329 -  $5^{\circ}\text{N}$  across the Pacific basin. The east west SST gradient is the same in both  
330 simulations between  $200^{\circ}$  -  $250^{\circ}\text{E}$ , however the AMOC off run profile shows the  
331 eastward shift, visible as the minima and maxima in SST being shifted (red line,  
332 lower right panel). SSTs in the AMOC off run are also vertically offset to slightly  
333 lower values.

334 Figure 8 shows fields of annual mean wind vector differences and their mean  
335 components across the Pacific integrated between  $5^{\circ}\text{S}$  -  $5^{\circ}\text{N}$ . The bottom right plot  
336 shows that the mean  $v$  wind component is positive (northward flow) east of  $240^{\circ}$

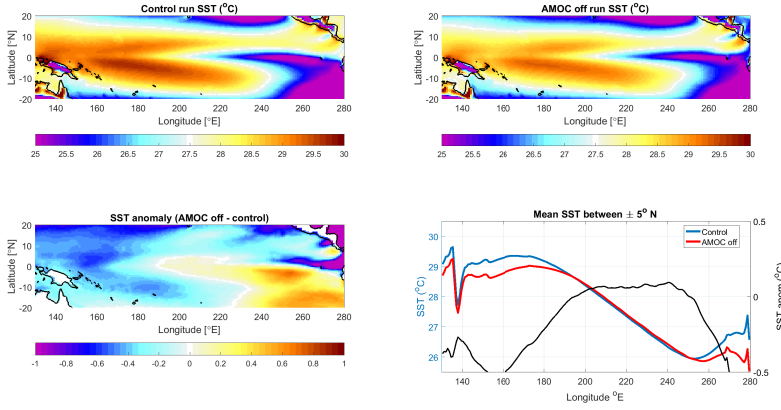


**Fig. 7** Annual means of sea surface temperature (SST) in both runs and their difference. Also plotted is the mean SST integrated across  $5^{\circ}\text{S} - 5^{\circ}\text{N}$ , control run (blue), AMOC off (red) and their difference, AMOC off - control (black). The gradient in SST between  $200^{\circ} - 250^{\circ}\text{E}$  is the same but is shifted slightly eastward visible in the anomaly (solid black line, lower right hand panel). The warm pool and western Pacific in the AMOC off run is cooler due to the anomalous flow of cooler waters from the northern hemisphere while the cold tongue is slightly warmer due to the reduced upwelling from the deeper thermocline. The eastern equatorial coast has a northern cooling due to the influence of the anomalously cold North Atlantic whose influence is via the atmosphere while the south eastern equatorial Pacific is warmer due to the reduced upwelling.

337 E and is reduced in the AMOC off run east of  $200^{\circ}\text{E}$ . This north blowing wind will  
 338 cause westward Ekman transport of the surface waters in the southern hemisphere  
 339 at the South America - equatorial east Pacific boundary and the upwelling of  
 340 cooler, deeper waters lifting the thermocline. As this northward component is  
 341 reduced in the AMOC off run a deeper thermocline is expected. Reduced upwelling  
 342 of cooler waters would also suggest warmer SSTs which are generally observed  
 343 (figure 7, lower left panel) particularly in the region of the east equatorial Pacific  
 344 south of the equator where anomalous ENSO variability is concentrated. There is a  
 345 localised anomalous cooling in the north east equatorial Pacific which results from  
 346 its proximity to the much anomalously colder north Atlantic. This strong localized  
 347 anomalous temperature dipole in the east Pacific will result in the anomalous north  
 348 to south wind and the reduction in Ekman transport off shore. The eastward shift  
 349 in the AMOC off annual mean equatorial Pacific state can also be seen from the  
 350 mean  $u$  wind component (figure 8, lower right panel, solid coloured lines).

Ekman transport,  $\mathbf{M} = (M_x, M_y)$  and its divergence are diagnosed from the annual mean surface wind fields using

$$M_x = \frac{\hat{\tau}_y}{f} \quad (1)$$

$$M_y = -\frac{\hat{\tau}_x}{f} \quad (2)$$

351 where  $f = 2\Omega \sin \phi$  is the Coriolis parameter,  $\Omega$  is the angular rotation rate of the  
 352 Earth, and  $\phi$  is the latitude. Wind stress components,  $\hat{\tau}_x, \hat{\tau}_y$  are diagnosed from  
 353 the annual mean wind speed components such that  $\hat{\tau}_x \propto u|u|, \hat{\tau}_y \propto v|v|$ . We will

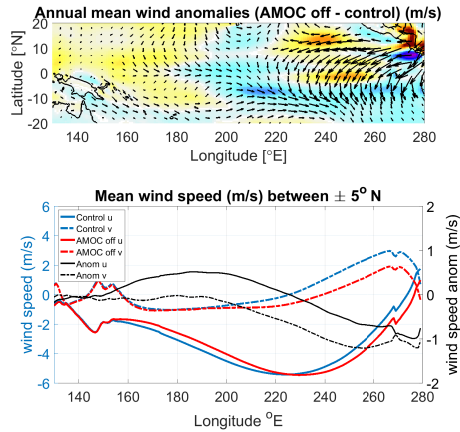


**Fig. 8** Annual mean surface wind anomalies. In the upper panel, anomalies in absolute wind speed are given in the colour plot and the anomalies in wind direction and magnitude are given by the vectors. The bottom panel is the mean of the  $u$  (eastward flow positive, solid line) and  $v$  (northward flow positive, dotted line) components between  $5^{\circ}\text{S} - 5^{\circ}\text{N}$  across the Pacific basin, the control run is blue, AMOC off red and the anomalies (AMOC off - control) of the wind components are in black. Dotted for  $v$  anomalies and solid for  $u$  anomalies.

354 only be interested in anomalies of  $\mathbf{M}$  so all constants such as  $2\Omega$  etc will be set  
 355 to 1. A divergence of Ekman transport will result in an upward vertical current  $w_E$   
 356 through conservation of mass ( $w_E$  is taken as positive upwards) and a shoaling of  
 357 the thermocline i.e.

$$\nabla \cdot \mathbf{M} = w_E. \quad (3)$$

358 We plot both the anomalous Ekman transport (represented by the vectors) be-  
 359 tween the two runs and its divergence (negative values indicate convergence and a  
 360 deepening thermocline, blue colours) in figure 9. Areas of anomalous Ekman trans-  
 361 port convergence in the eastern equatorial Pacific (blue colours) and an anoma-  
 362 lous eastward Ekman transport in the southern hemisphere east of  $200^{\circ}\text{E}$  (Ekman  
 363 transport direction and magnitude are given by the vectors) can be seen. The  
 364 transport is divergent in the western equatorial region (red colours).

#### 365 4.1.2 Eastward shift in variability

366 The wind-evaporation-SST (WES) feedback (Xie and Philander 1994) may influ-  
 367 ence ENSO variability by altering the rate at which SSTs are damped by evapo-  
 368 rative fluxes. Anomalies in evaporation are correlated with SST, wind speed and  
 369 humidity anomalies that are present in the subtropics. Near the equator however,  
 370 it appears that changes in Ekman transport and pumping are dominant. In figure  
 371 10 we show variability in latent heat flux is shifted eastward by linearly regress-  
 372 ing SST anomalies in the Niño 3 against deseasonalised monthly spatial fields  
 373 of upward latent heat flux. We have also linearly regressed Niño 3 SST against  
 374 thermocline depth and  $u$  wind which show the same eastward shift (figures not  
 375 shown).

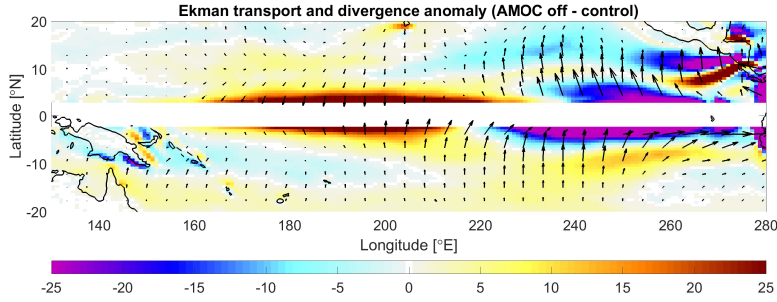


**Fig. 9** Annual mean Ekman transport anomaly field and its divergence diagnosed from annual mean  $u$  and  $v$  wind component anomalies. Divergence of Ekman transport,  $\nabla \cdot \mathbf{M}$  is the colour plot, negative values indicate downwelling and deepening thermocline. Vectors give the Ekman transport direction and magnitude. Note these plots have all constants set to 1 and are intended only to show changes in magnitude and direction. Ekman transport is not calculated in the  $\pm 2^\circ$  N band of latitudes due to the Coriolis parameter  $f$  being very small here.

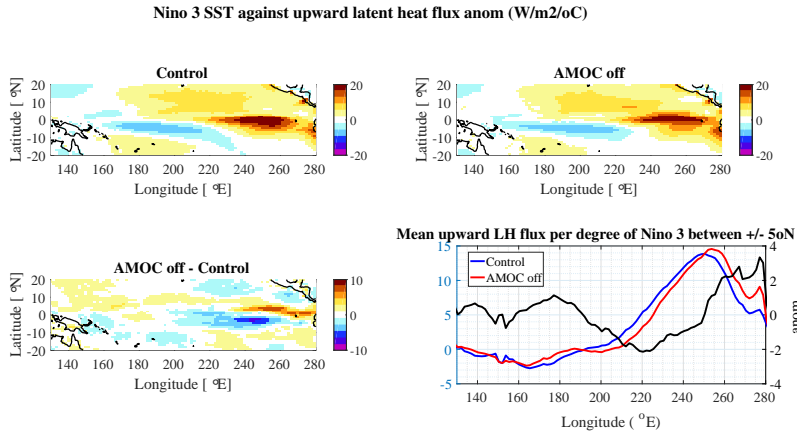


**Fig. 10** Linear regression of Niño 3 SST against monthly spatial fields of upward latent heat flux ( $\text{W/m}^2/^\circ\text{C}$ ). The upper left panel is the control run, upper right is the AMOC off run, bottom left is the difference. The bottom right is the mean between  $\pm 5^\circ\text{N}$ , the blue line is the control run, the red is the AMOC off run and the black line is their difference.

## 376 4.2 Shift to longer ENSO period

### 377 4.2.1 Increased thermocline depth in eastern equatorial Pacific

378 We expect the anomalous divergence (convergence) of Ekman transport to cause  
 379 shoaling (deepening) of the thermocline. In figure 11 we plot the differences in  
 380 thermocline depth that are significant at the 99% confidence level and the ther-

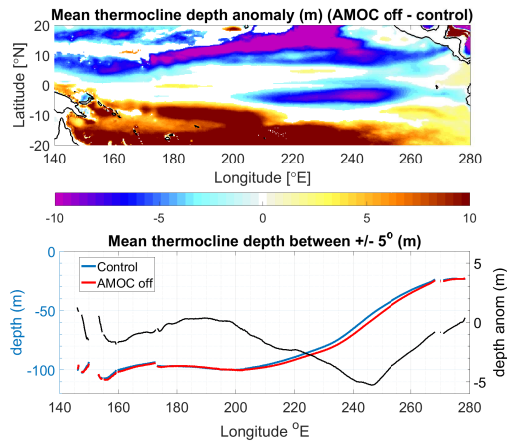


**Fig. 11** Mean thermocline depth anomaly spatial patterns in the top panel between AMOC off and control run. Increasing depth means increasingly negative values. We have only plotted the differences that are significant above the 99% confidence level using a t-test. The thermocline is deeper in the eastern equatorial Pacific where most of the ENSO variability occurs. The lower panel shows annual mean thermocline depth across the Pacific basin integrated between  $5^{\circ}\text{S} - 5^{\circ}\text{N}$  in the control run (blue) and AMOC off run (red) and their difference (AMOC off - control) in black.

381 mocline depth in both runs integrated between  $5^{\circ}\text{S} - 5^{\circ}\text{N}$  across the Pacific basin.  
 382 Differences were tested for significance by performing a t-test on the spatial fields  
 383 of the annual mean thermocline depth in each run. The difference in annual mean  
 384 thermocline depth change is of the same order as the ocean vertical resolution  
 385 however it is significant. One sees a deepening of the thermocline in the east Pa-  
 386 cific concentrated in the region of large ENSO variability as expected from the  
 387 changes in the wind fields and the Ekman transport divergence. This increased  
 388 thermocline depth in the east will increase the heat capacity in this region.

389 The deeper thermocline in the east equatorial Pacific should also mean this  
 390 region will respond slower to changes in SATs or radiative surface fluxes due to  
 391 the increased heat capacity. Using a simple, analytically tractable linear ENSO  
 392 model (Jin (1997)'s recharge oscillator) to qualitatively understand the behaviour  
 393 of the much more complex climate model, we demonstrate the increased SST  
 394 relaxation time can result in increased ENSO period.

#### 395 4.2.2 Jin (1997)'s recharge oscillator

This model consists of two coupled variables, the thermocline depth anomaly in the west Pacific  $h_W$  and the SST anomaly in the east of the Pacific  $T_E$  which we take to be the Niño 3 SST anomaly or equivalently the leading EOF SST projection. Essentially, it models the slow ENSO dynamics as a damped harmonic oscillator excited by fast, random, atmospheric weather noise. We give the equations without detailed discussion or justification, full details can be found in Jin (1997). The recharge oscillator is completely described by (overdots denote differentiation with

respect to time)

$$\begin{aligned}\dot{h}_W &= -rh_W - \alpha b T_E - \alpha \xi_1 \\ \dot{T}_E &= -c T_E + \gamma b T_E + \gamma h_W + \gamma \xi_1 + \xi_2\end{aligned}\quad (4)$$

396 The parameter  $r$  is the relaxation rate of the western Pacific thermocline anomaly  
 397 that collectively represents the damping of the upper ocean through mixing and  
 398 energy loss at the boundaries through propagation of Kelvin and Rossby waves.  $\alpha$   
 399 is a coupling constant for Sverdrup transport and wind stress and is set to  $\alpha = r/2$   
 400 to give a mean thermocline anomaly of zero.  $b$  is a coupling constant that relates  
 401 east to west wind stress to eastern Pacific SST anomalies when in equilibrium i.e.  
 402 a positive  $T_E$  gives rise to an anomalous west to east wind stress. The relaxation  
 403 rate of the eastern Pacific SST anomaly towards climatology is given by  $c$ .  $c$  will  
 404 be reduced by an increased thermocline depth and this is the parameter changed  
 405 later on in the section.  $\gamma$  represents thermocline depth-SST feedback and  $\xi_1$  and  
 406  $\xi_2$  are stochastic forcing by random wind stress and random heating respectively.  
 407 Both are represented by random variables with Gaussian distributions and with  
 408 respective standard deviations  $\sigma_1$  and  $\sigma_2$ .

409 The two first order ordinary differential equations (ODE) (equations 4) can be  
 410 rewritten as a single second order ODE of only variable  $T_E$  in the standard form  
 411 of a forced damped harmonic oscillator. This form will be most convenient for our  
 412 purpose.

$$\ddot{T}_E + 2\delta\dot{T}_E + \omega_0^2 T_E = \tilde{\xi}(t) \quad (5)$$

413  $\omega_0^2 = \alpha b \gamma - r R$  and the term on the right hand side is the new stochastic forcing  
 414 term given by  $\tilde{\xi} = \gamma(r - \alpha)\xi_1 + r\xi_2 + \gamma\xi_1 + \xi_2$ . In the absence of random forcing  
 415 ( $\tilde{\xi}(t) = 0$ ) one finds the eastern SST anomaly  $T_E$  solution has damping  $\delta$  given by

$$\delta = -\frac{1}{2}(R - r) \quad (6)$$

416 where  $R = \gamma b - c$  and angular frequency of the oscillation,  $\omega$ ,

$$\omega = \sqrt{\omega_0^2 - \delta^2}. \quad (7)$$

#### 417 4.2.3 Parameter values

418 Jin's recharge oscillator only distinguishes east and west and does not model spatial  
 419 changes only changes in amplitude and frequency. It also only models the slow  
 420 ENSO dynamics. Although the ENSO spatial structure changes in the AMOC  
 421 off run it is a small change (an eastward shift in the EOF) and the division in  
 422 the simple model between east and west is still appropriate. In fact very little  
 423 has changed between the two runs in the equatorial Pacific implying many of the  
 424 simple model parameters are equal for the two HadGEM3 runs. Apart from the  
 425 eastward shift in ENSO and the mean state, the other change is the mean depth of  
 426 the thermocline in the eastern equatorial Pacific. This depth change should affect  
 427  $c$ , the relaxation time of eastern Pacific SST anomalies.  $\delta$ , the decay rate of the  
 428 ENSO oscillation and  $\omega$  the ENSO oscillation frequency (both functions of  $c$ ) are  
 429 the other parameters that are different between the runs and these two parameters  
 430 are directly measured from the autocorrelation function.

Where possible, we fit the model parameters to those inferred in the HadGEM3 model runs otherwise we use Jin (1997)'s original values. The original parameter values used are  $\gamma = 0.0187^\circ\text{C m}^{-1} \text{ mth}^{-1}$  and  $r = 1/8 \text{ mth}^{-1}$  giving  $\alpha = 1/16 \text{ mth}^{-1}$  and these are the same for both AMOC off and control runs.

Parameter  $b$  is estimated from HadGEM3 and it is approximately the same in both AMOC off and control runs. It is a measure of east to west thermocline depth difference when in balance with the west to east wind stress resulting from an east to west temperature difference. Specifically it comes from the following equation in Jin's original paper

$$h_E = h_W + \hat{\tau}_x \quad (8)$$

$\hat{\tau}_x$  is proportional to the zonally integrated wind stress anomaly which is parameterized as  $\hat{\tau}_x = bT_E$  assuming  $T_W = 0$  i.e. there is no western Pacific SST anomaly, all the SST change is in the east and this east to west temperature difference produces an west to east wind stress. This relation assumes the pressure gradient force associated with the difference in east to west thermocline depth is in balance with the wind stress force resulting from the east to west temperature difference.  $b$  is difficult to estimate from regressions of east to west thermocline depth difference versus east to west temperature difference using the HadGEM3 simulations as the model never reaches a true equilibrium between the thermocline depth difference and the wind stress at a given time due to the different adjustment time scales (and therefore lags) of the SST and thermocline depths in the east and west Pacific. We have performed these regressions however poor correlation ( $r^2 < 0.5$ ) and time lag between the variables were found resulting in low values ( $10 \text{ m}/^\circ\text{C}$ ) of the coupling  $b$ . Instead we use the mean state (mean east to west thermocline depth difference versus mean east to west SST difference) to estimate this parameter as this should be a good estimate of the equilibrium state. In Jin's original paper,  $b = b_0\mu$  and  $b_0$  is set to give 50 m of thermocline depth difference per  $1^\circ\text{C}$  of east-west SST difference and notes this may be high end estimation of  $b$ . To study the model sensitivity to the value of  $b$ , he introduces the adjustable parameter  $\mu$  to span high and low couplings. From figure 7 and 11 we estimate  $b$  to be 80 m of east-west thermocline difference per  $3^\circ \text{C}$ . This corresponds to a value of  $\mu \approx 0.5$ .

The damping parameter,  $\delta$ , can be estimated from the autocorrelation function in figure 6 and is different in each run. The  $T_E(t)$  solutions of equation 5 are underdamped and oscillatory showing decaying oscillations of frequency  $\omega$  from their initial value with an  $e$ -folding decay time scale ('the oscillation decay envelope') of  $\tau = 1/\delta$ . With the introduction of stochastic forcing by  $\xi$  the damped oscillator will be continually perturbed and the resulting response will be a superposition of all of the individual decaying oscillation responses. The autocorrelation function allows one to see this response when the ENSO mode is subjected to this type of stochastic forcing (figure 6). It is apparent from this figure that the AMOC off run is less damped (longer  $\tau$ ) than the control run as the oscillations decay more slowly. We can estimate these decay  $e$ -folding timescales (and equivalently  $\delta$ ) from these plots. We estimate the timescale in the control run to be  $\tau_c \approx [1.4, 1.7]$  yrs and  $\tau_o \approx [2.3, 2.9]$  yrs in the AMOC off run from figure 6 by fitting a decay envelope of the form  $e^{-t/\tau}$  to the peaks in the autocorrelation function.

As mentioned previously,  $c$ , the relaxation rate towards climatology of  $T_E$  will be reduced by an increase in eastern Pacific thermocline mean depth. Assuming all

477 the change in  $\delta$  in the two runs is due to a change in  $c$  we can estimate  $c$  using the  
 478 values of  $\tau$  and the inferred constants from equation 6. We find  $1/c_c = [2.16, 2.27]$   
 479 mths in the control run and  $1/c_o = [2.41, 2.50]$  mths in the AMOC off run roughly  
 480 a [6%,13%] decrease relative to the control run in  $c$ . This is slightly longer, but  
 481 comparable to Jin’s original value of 2 months. As an independent consistency  
 482 check,  $c$  should be inversely proportional to the change in thermocline depth,  $d$   
 483 i.e.  $c_o/c_c \approx d_c/d_o$ . From figure 11 the mean thermocline depth anomaly in the  
 484 eastern Pacific region is about 10 m and the mean depth is about 60 m so the  
 485 change in  $d_c/d_o$  is roughly a 14% decrease so consistent with the change in  $c$   
 486 inferred from the change in  $\delta$ .

#### 487 4.2.4 Implied ENSO period from changes in $c$ and sensitivity to parameter values

488 With these inferred values of the simple model’s constants we can calculate the  
 489 implied oscillation frequency (or equivalently period,  $P = 2\pi/\omega$ ) for each run us-  
 490 ing equation 7. The calculated period of the control run is  $P_c = [40, 41]$  months  
 491 compared to the 38 month period estimated for HadGEM3 from the autocorrela-  
 492 tion function. The calculated period of the AMOC off run is  $P_o = [43, 44]$  months  
 493 compared to HadGEM3’s 45 month period i.e. the change in mean thermocline  
 494 depth results in  $P_o > P_c$ .

495 We have studied the sensitivity of the result  $P_o > P_c$  due to changes in ther-  
 496 mocline depth on the value of the various parameters in Jin (1997)’s model.

497 The sensitivity to the value of  $b = b_0\mu$  is made by varying  $\mu$  to span very low  
 498 wind stress-thermocline depth difference coupling ( $\mu = 0.2, b = 10 \text{ m}^\circ\text{C}^{-1}$ ) to high  
 499 coupling ( $\mu = 1, b = 50 \text{ m}^\circ\text{C}^{-1}$ ). Throughout the range of high to low couplings  
 500  $P_o > P_c$  although absolute numbers change from  $P_c \approx 77$  months and  $P_o \approx 115$   
 501 months at  $\mu = 0.2$  to  $P_c \approx 27$  months and  $P_o \approx 28$  months at  $\mu = 1$ . These values  
 502 correspond to proportional decreases in  $c_o/c_c$  of 25% ( $\mu = 0.2$ ) to 5% ( $\mu = 1$ ).  
 503 Values of around  $\mu \sim 0.5$  give reasonable agreement with HadGEM3 results.

504 In the equations for  $\delta$  and  $\omega$ ,  $\gamma$  and  $b$  never appear on their own, only as the  
 505 product  $\gamma b$ . Therefore the sensitivity analysis of  $b$  is equivalent to the sensitivity  
 506 of  $\gamma$  relating to the SST-thermocline depth feedback.

507 We have also tested the sensitivity of the result to the remaining parameter  $r$ ,  
 508 related to the adjustment time of the thermocline anomaly in the western Pacific.  
 509 Fixing  $r$  also fixes  $\alpha$  which parameterizes the adjustment by Sverdrup transport.  
 510 By making  $r = \mu_r r_0$  ( $r_0 = 1/8 \text{ mth}^{-1}$ ),  $\mu_r$  is varied between 0 and 2 to span  
 511 long and short adjustment times. Provided  $r > 1/24 \text{ mth}^{-1}$  corresponding to  
 512  $\mu_r = 0.34$ ,  $P_o > P_c$ . At  $r \sim 1/24$  the two ENSO periods are the same, having the  
 513 value  $P_c = P_o \sim 63$  months. The ratio  $c_o/c_c$  is relatively insensitive to the value  
 514 of  $r$  with proportional decreases of 8% for low values of  $r$  (slow adjustment of the  
 515 thermocline anomaly) and 13% for high values (fast adjustment).

516 This demonstrates an increase in the relaxation time of the eastern Pacific  
 517 anomaly,  $1/c$ , in this region of the recharge oscillator’s parameter space results in  
 518 an increase in ENSO period.

519 4.3 Simultaneous decreases in damping and stochastic forcing resulting in little  
520 change in ENSO amplitude

521 Regarding ENSO as a stochastically forced under-damped harmonic oscillator, the  
522 decreased damping rate in the AMOC off run should have some other observable  
523 consequences: (i) Peaks in the power spectra should be narrower and higher and lo-  
524 cated at frequency  $\sqrt{\omega^2 - \delta^2}$ . (ii) Oscillations should have a longer coherence time  
525 in the autocorrelation function and (iii) given the same magnitude of stochastic  
526 forcing, the mean amplitude of the response should be larger. (i) and (ii) are ob-  
527 served in figure 6 however (iii), the amplitudes of the ENSO modes in each run are  
528 roughly the same in the control and AMOC off runs (table 1, Niño 3 SST anomaly  
529 or EOF standard deviation).

530 Since these are conceptual arguments additional approximations on the stochas-  
531 tic forcing of equation 5 are made. That is,  $\xi$  is taken to be a Gaussian random  
532 variable with standard deviation  $\tilde{\sigma}$  rather than having separate  $\xi_1$  and  $\xi_2$  terms  
533 and their time derivatives for ease of interpretation. (A full calculation brings the  
534 following estimates of  $\text{std}(T_E)$  in each run closer together but adds nothing but  
535 complication to the points following.) According to this model, the ENSO standard  
536 deviation should be proportional to

$$\text{std}(T_E) \propto \frac{\tilde{\sigma}}{\sqrt{\delta\omega}}. \quad (9)$$

537 That is, ENSO amplitude is a function of the magnitude of the noise forcing,  $\tilde{\sigma}$ , the  
538 damping  $\delta$  and angular frequency  $\omega$ . This relation implies that if the magnitude of  
539 the noisy forcing was the same for both AMOC off and control runs (superscript  
540  $o$  and  $c$  respectively),  $\tilde{\sigma}^c = \tilde{\sigma}^o$ , one should see  $\frac{\text{std}(T_E^o)}{\text{std}(T_E^c)} = [1.27, 1.57]$  i.e. 27 - 57  
541 % higher ENSO amplitude in the AMOC off run, a significant change that is not  
542 observed in the model simulations. (We have used the HadGEM3 observed values  
543 of  $\omega$  and  $\delta$  in each run for this calculation.) Another possibility is the stochastic  
544 forcing terms are significantly smaller in magnitude in the AMOC off run to offset  
545 the increased tendency to oscillate from the reduced damping. Using this as a  
546 hypothesis and setting the standard deviations in  $T_E$  to be equal for the inferred  
547 parameter sets for each of the simulations implies  $\tilde{\sigma}^o/\tilde{\sigma}^c$  should be  $[0.64, 0.79]$   
548 times smaller in the AMOC off run.

549 We look directly for this change in stochastic forcing guided by the terms  $\xi_1$   
550 (random wind stress) and  $\xi_2$  (random heating in the east Pacific) in equation 4  
551 by linearly regressing deseasonalized proxies for  $\xi_1$  and  $\xi_2$  against the the Niño 3  
552 SST anomaly. The regression is done to remove the dependence of these proxies  
553 on ENSO. The standard deviation of the residual of these regressions is attributed  
554 as the stochastic term. As a proxy for  $\xi_1$  (random wind stress), the square of wind  
555 speed in the region overlapped by the Niño 3.4 and Niño 4 regions is taken. The  
556 residual standard deviation is found to be 0.67 times smaller in the AMOC off run.  
557 The proxy for  $\xi_2$  (random heating in the east Pacific) is taken to be net surface  
558 shortwave flux in the Niño 3 region. The residual standard deviation is 0.86 times  
559 smaller in the AMOC off run. Both of these proxies are close to the estimated range  
560 suggesting the reduction in stochastic forcing could offset the decreased damping  
561 with the result of little change in ENSO amplitude.

562 The above analysis points towards the lack of change of amplitude in the  
563 AMOC off run being a result of a reduction in stochastic forcing being offset by

564 a reduction in the damping of SST anomalies. We note however that there are  
565 multiple frameworks for assessing the contribution of individual ENSO processes  
566 and feedbacks to the amplitude of events in the real world and in models. This  
567 is just one and other methods, be they linear or non-linear, might yield different  
568 conclusions. A comprehensive comparison of all methods of quantifying ENSO  
569 feedbacks is not possible here, hence we present this analysis as support, but not  
570 proof, of the hypothesis.

## 571 **5 Discussion**

572 There have been three other ENSO studies of hosed coupled GCMs that we are  
573 aware of, those of Timmerman et al (2007), Dong and Sutton (2007) and Svendsen  
574 et al (2014). Timmerman et al (2007) used five different CMIP3 era models (GFDL  
575 CM2.1, NCAR CCSM2, NCAR CCSM3, MPI-OM1 and HadCM3) while Dong and  
576 Sutton (2007) looked in more detail at a single model (HadCM3). All 5 models in  
577 Timmerman et al (2007) had significantly increased ENSO amplitudes as measured  
578 by the power spectra of the SST anomalies in the Niño 3 region. We do not find  
579 significant differences in amplitudes in HadGEM3 although peaks in its spectra  
580 were narrower and more defined suggesting that HadGEM3 has a decreased ENSO  
581 damping when the AMOC is off. Reduced damping may be the likely cause of the  
582 increased amplitude in the CMIP3 models although this would have to be confirmed  
583 via more persistent oscillations in their autocorrelation functions. However, the  
584 increase of peaks without broadening in the CMIP3 model's power spectra suggest  
585 their ENSOs become more periodic and less damped. If the increase in the peaks  
586 were due to increased broadband stochastic forcing one would expect the whole  
587 spectrum to be amplified.

588 HadCM3 may be considered a CMIP3-class model. In general, CMIP5-class  
589 models show an improvement in terms of representing both the properties of ENSO  
590 (amplitude, frequency, spatial pattern) and the physical processes and feedbacks  
591 which are responsible for generating and maintaining the oscillation (Bellenger  
592 et al 2014). However, there still exists a wide diversity of ENSO properties and  
593 processes in the CMIP5 models which has led to a number of different efforts to  
594 coordinate and improve models (Guilyardi et al 2016). HadGEM3 has been devel-  
595 oped to be submitted to CMIP6 and, in this configuration, represents a significant  
596 enhancement in resolution. The diagnostics of ENSO presented here indicate a  
597 ability to simulate the mode that is competitive with other models of similar res-  
598 olution. Further work is underway to assess processes and to isolate the impact of  
599 resolution (Haarsma et al 2016).

600 In 4 out of the 5 CMIP3 models a significant weakening in the eastern tropical  
601 Pacific annual cycle was also found (the AMOC off run annual cycle peaks are  
602 between 0.56 and 0.71 times smaller than the control as estimated from Niño 3  
603 power spectra, figure 6 in Timmerman et al (2007)), the exception being MPI-OM1  
604 where it was approximately the same. We also find a significant weakening in the  
605 eastern tropical Pacific annual cycle in HadGEM3 (figure not shown). The peak  
606 in the Niño 3 SST power spectrum is peak is 0.63 times smaller in the AMOC  
607 off run, about the same as the decrease found in the stochastic forcing. Guilyardi  
608 (2006) reported an inverse relationship between ENSO amplitude and strength of  
609 the seasonal cycle for CMIP3 models. HadGEM3 does not follow this relationship.

610 Thermocline depth and  $u$  wind anomaly patterns in the tropical Pacific dif-  
 611 fer between the CMIP3 models. HadCM3 and GFDL CM2.1 showing thermocline  
 612 shoaling in the western Pacific and deepening in the east. Across the entire tropi-  
 613 cal Pacific CCSM2 and CCSM3 show deepening while MPI-OM1 has significant  
 614 thermocline shoaling. Wind anomaly patterns reflect the changes in thermocline  
 615 depth. The simulations reported here are most similar to HadCM3 and GFDL  
 616 CM2.1 with respect to the thermocline and  $u$  wind change patterns although  
 617 there is no thermocline shoaling in the western Pacific in HadGEM3, it remains  
 618 approximately unchanged in this model. In all models apart from MPI-OM1 there  
 619 is a deeper thermocline in the eastern Pacific.

620 Dong and Sutton (2007) look at the HadCM3 runs in more detail. It is an  
 621 earlier incarnation of the model used in this study and these simulations have a  
 622 lot of similarity with HadGEM3 even though the ocean model is very different.  
 623 In particular they find the ENSO mode is shifted eastward and the annual cycle  
 624 is also reduced (it is about 0.56 times smaller as estimated from Niño 3 power  
 625 spectra, figure 6 in Timmerman et al (2007) which is comparable to 0.63 found  
 626 in HadGEM3). However ENSO amplitude increased significantly to 1.3 times the  
 627 control run in HadCM3.

628 From the power spectra in Timmerman et al (2007) it appears that there is  
 629 no change in ENSO period for most CMIP3 models. Only GFDL CM2.1 has a  
 630 shorter ENSO period in the AMOC off run. HadGEM3 has an increased period.

631 Using Jin (1997)'s stochastically forced damped harmonic oscillator model of  
 632 the slow ENSO dynamics we argued how one could understand the results pre-  
 633 sented in this manuscript. That is, the dominant effect is the deeper thermocline  
 634 in the eastern Pacific increasing the eastern Pacific ocean relaxation time and so  
 635 increasing the period of the ENSO cycle. We fitted these model parameters from  
 636 the HadGEM3 simulations of thermocline slope and estimated the ENSO damp-  
 637 ing rate  $\delta$  from the autocorrelation functions of the ENSO mode time series. The  
 638 estimated damping rate allowed us to infer the eastern Pacific relaxation rate and  
 639 this was consistent with the observed change in thermocline depth in this region.  
 640 Jin (1997)'s model makes predictions as to what one should observe in the more  
 641 complex model, that is, narrower more defined peaks in the power spectra and a  
 642 lengthened ENSO period which were observed.

643 Roughly, ENSO amplitude in Jin (1997)'s model should be  $\text{std}(T_E) \propto \frac{\tilde{\sigma}}{\sqrt{\delta\omega}}$   
 644 where  $\tilde{\sigma}$  is the standard deviation of the stochastic forcing (the actual relation  
 645 is a bit more complicated in Jin's model due to the way the stochastic forcing is  
 646 added to the model equations). This means reduced damping should give larger  
 647 ENSO amplitudes if  $\omega$  and  $\tilde{\sigma}$  are fixed. Alternatively, reductions in stochastic forc-  
 648 ing along with decreased damping can give rise to the same ENSO amplitude. If  
 649  $\tilde{\sigma}$  is proportional to the amplitude of the annual cycle in the eastern Pacific in  
 650 other models (as it was in HadGEM3) this could also explain the increased ampli-  
 651 tude found in the other models i.e. the reduction in stochastic forcing magnitude is  
 652 outweighed by the decrease in damping. This would have to be confirmed via auto-  
 653 correlation functions and measurements of stochastic forcing in the other models.  
 654 As argued above, from the CMIP3 model's power spectra it seems likely that their  
 655 ENSOs become less damped and more periodic. If confirmed this would imply  
 656 the resulting ENSO amplitude could depend heavily on just three parameters; the  
 657 measured  $\delta$ ,  $\omega$  and  $\tilde{\sigma}$  in each CGCM.

658 Jin’s simple linear stochastically forced damped oscillator model explains many  
 659 of the features seen in these simulations. We should also mention this model has  
 660 a nonlinear extension which also supports self sustained oscillations (limit cycles)  
 661 when the wind stress temperature anomaly coupling becomes large through the  $b$   
 662 parameter (Jin 1997). If ENSO were a noisy self sustained, rather than a stochas-  
 663 tically excited damped oscillation, power spectra and autocorrelation functions  
 664 would look very similar although the amplitude sensitivity to stochastic forcing  
 665 would be reduced.

666 Although a shutdown of the AMOC is thought unlikely in the 21st century,  
 667 weakening is expected. The AMOC also has natural variability in its strength as  
 668 witnessed by the Atlantic multidecadal oscillation. Yu et al (2015) have suggested  
 669 a link between AMO and El Niño location, stronger AMOC leading to more central  
 670 El Niño events and conversely weaker AMOC to more eastern El Niño events, very  
 671 similar to our findings.

## 672 6 Conclusion

673 In conclusion we have studied the changes in ENSO when the AMOC is in the off  
 674 state in a high resolution, eddy resolving coupled CGCM and proposed a simple  
 675 mechanism for the changes in the slow ENSO dynamics. We found the ENSO  
 676 spatial pattern is shifted eastward and to longer oscillation periods although the  
 677 its amplitude and distribution of SST anomalies remains approximately the same.  
 678 The mechanism to explain these changes is as follows:

- 679 – When the AMOC is off an anomalous cold north-warm south hemisphere tem-  
 680 perature dipole results (figure 2).
- 681 – This induces a north to south anomalous surface wind (particularly strong near  
 682 the South American coast because of the proximity to the N Atlantic, figure  
 683 8, lower panel, dotted lines).
- 684 – The anomalous surface wind causes a wind stress on the ocean surface and  
 685 leads to an anomalous eastward Ekman transport just south of the equator  
 686 shifting the mean equatorial Pacific state and with it the ENSO mode east  
 687 (figure 9).
- 688 – Anomalous convergences in Ekman transport close to the south American coast  
 689 deepen the thermocline in the east Pacific, increasing the temperature anomaly  
 690 relaxation time and therefore lengthening the ENSO period (figure 11).

691 The increase in ENSO period is backed up using a simple model of ENSO as a  
 692 stochastically forced damped oscillator. This model makes additional predictions  
 693 including a narrower spectral peak, more regular oscillation (decreased oscillation  
 694 damping) and reduced stochastic forcing which are observed.

695 Previous studies with older, lower resolution CMIP3 era models show similar  
 696 behaviour, particularly an earlier generation of this model, HadCM3. However,  
 697 they all show increased ENSO amplitude. Using the simple model, one can poten-  
 698 tially understand the differing responses in the slow ENSO dynamics as a com-  
 699 petition between the decrease in damping tending to increase amplitude and the  
 700 decrease in forcing tending to decrease the amplitude. In HadGEM3 the decrease  
 701 in damping is being offset by the reduction in forcing. From equation 9, this would

imply the resulting ENSO amplitude could depend on just the damping  $\delta$ , the frequency  $\omega$  and magnitude of the stochastic forcing  $\tilde{\sigma}$  in each CGCM.

**Acknowledgements** The research leading to these results has received funding from the European Union Seventh Framework Programme FP7/2007-2013 under grant agreement no. 603864 (HELIX). MC acknowledges funding from NE/N018486/1. We would also like to thank Richard Betts, Peter Cox, Matt Hawcroft and Laura Jackson for useful conversations.

## References

- Ashok K, Yamagata T (2009) The El Niño with a difference. *Nature* 461:481–484
- Bellenger H, Guilyardi E, Leloup J, Lengaigne M, Vialard J (2014) ENSO representation in climate models: from CMIP3 to CMIP5. *Clim Dyn* 42:1999–2018
- Clement AC, Peterson LC (2006) Mechanisms of abrupt climate change of the last glacial period. *Rev Geophys* 46:RG4002
- Collins M, An SI, Cai W, Ganachaud A, Guilyardi E, Jin FF, Jochum M, Lengaigne M, Power S, Timmermann A, Vecchi G, Wittenberg A (2010) The impact of global warming on the tropical Pacific Ocean and El Niño. *Nat Geosci* 3:391
- Collins M, Knutti R, Arblaster J, Dufresne JL, Fichefet T, Friedlingstein P, Gao X, Gutowski WJ, Johns T, Krinner G, Shongwe M, Tebaldi C, Weaver AJ, Wehner M (2013) Long-term climate change: projections, commitments and irreversibility. In: Stocker TF, D DQ, Plattner GK, Tignor M, Allen SK, Boschung J, Nauels A, Xia Y, V VB, Midgley PM (eds) *Climate change 2013: the physical science basis. Contribution of working group I to the fifth assessment report of the Intergovernmental Panel on Climate Change*, Cambridge University Press, Cambridge
- Demory ME, Vidale P, Roberts M, Berrisfor P, Strachan J, Schiemann R, Mizielinski M (2013) The role of horizontal resolution in simulating drivers of the global hydrological cycle. *Clim Dyn* 1:25
- Dong B, Sutton RT (2007) Enhancement of ENSO variability by a weakened Atlantic thermohaline circulation in a coupled GCM. *J Climate* 20:4920–4939
- Guilyardi E (2006) El Niño-mean state-seasonal cycle interactions in a multi-model ensemble. *Clim Dyn* 26:329–348
- Guilyardi E, Wittenberg A, Balmaseda M, Cai W, Collin M, McPhaden M, Watanabe M, Yeh S (2016) Forth CLIVAR workshop on the evaluation of ENSO processes in climate models. *ENSO in a changing climate. B Am Meteorol Soc* 97:817–820
- Haarsma RJ, Roberts M, Vidale PL, Senior CA, Bellucci A, Bao Q, Chang P, Corti S, Fučkar NS, Guemas V, von Hardenberg J, Hazeleger W, Kodama C, Koenigk T, Leung LR, Lu J, Luo JJ, Mao J, Mizielinski MS, Mizuta R, Nobre P, Satoh M, Scoccimarro E, Semmler T, Small J, von Storch JS (2016) High resolution model intercomparison project (highResMIP). *Geosci Model Dev* 9:4185–4208
- Hewitt HT, Copsey D, Culverwell ID, Harris CM, Hill RSR, Keen AB, McLaren AJ, Hunke EC (2011) Design and implementation of the infrastructure of HadGEM3: the next generation Met Office climate modelling system. *Geosci Model Dev* 4:223–253
- Hunke EC, Lipscomb WH (2010) CICE: The Los Alamos sea-ice model. documentation and user manual, version 4.1. Tech. Rep. LA-CC-06-012, Los Alamos National Laboratory
- Jackson LC, Kahana R, Graham T, Ringer MA, Woollings T, Mecking JV, Wood RA (2015) Global and European climate impacts of a slowdown of the AMOC in a high resolution GCM. *Clim Dyn* 45:3299–3316
- Jin FF (1997) An equatorial ocean recharge paradigm for ENSO. part I: Conceptual model. *J Atmos Sci* 54:811
- Madec G (2008) NEMO ocean engine. Tech. Rep. 27, Note du Pole de modelisation
- Marotzke J, Willebrand J (1991) Multiple equilibria of the thermohaline circulation. *J Phys Oceanogr* 21:1372–1385
- Mecking JV, Drijfhout SS, Jackson LC, Graham T (2016) Stable AMOC off state in an eddy-permitting coupled climate model. *Clim Dyn* doi:10.1007/s00382-016-2975-0:1–16
- Megann A, Storkey D, Aksenov Y, Alderson S, Calvert D, Graham T, Hyder P, Siddorn J, Sinha B (2013) GO5.0: The joint NERC-Met Office NEMO global ocean model for use in coupled and forced applications. *Geosci Model Dev* 6:5747–5799

- 757 North GR, Bell TL, Calahan RF, Moeng FJ (1995) Sampling errors in the estimation of  
758 empirical orthogonal functions. *Mon Wea Rev* 110:699–706
- 759 Rahmstorf S (2002) Ocean circulation and climate during the past 120,000 years. *Nature*  
760 419:207–214
- 761 Rahmstorf S, Crucifix M, Ganopolski A, Goosse H, Kamenkovich I, Knutti R, Lohmann G,  
762 Marsh R, Mysak LA, Wang Z, Weaver AJ (2005) Thermohaline circulation hysteresis: A  
763 model intercomparison. *Geophys Res Lett* 32:L23,605
- 764 Rooth C (1982) Hydrology and ocean circulation. *Prog Oceanogr* 11:131–149
- 765 Stommel H (1961) Thermohaline convection with two stable regimes of flow. *Tellus* 13:224–230
- 766 Stouffer RJ, Yin J, Gregory JM, Dixon KW, Spelman MJ, Hurlin W, Weaver AJ, Eby M,  
767 Flato GM, Hasumi H, Hu A, Jungclaus JH, Kamenkovich IV, Levermann A, Montoya  
768 M, Murakami S, Nawrath S, Oka A, Peltier WR, Robitaille DY, Sokolov A, Vettoretti G,  
769 Weber SL (2006) Investigating the causes of the response of the thermohaline circulation  
770 to past and future climate changes. *J Clim* 19:1365–1387
- 771 Svendsen L, Kvamstø NG, Keenlyside N (2014) Weakening AMOC connects equatorial Atlantic  
772 and Pacific interannual variability. *Clim Dyn* 43:2931–2941
- 773 Timmerman A, Okumura Y, An SI, Clement A, Dong B, Guilyardi E, Hu A, Jungclaus JH,  
774 Renold M, Stocker TF, Stouffer RJ, Sutton R, Xie SP, Yin J (2007) The influence of a  
775 weakening of the Atlantic meridional overturning circulation on ENSO. *J Clim* 20:4899–  
776 4919
- 777 Vellinga M, Wood RA (2002) Global climatic impacts of a collapse of the atlantic thermohaline  
778 circulation. *Clim Change* 54:43–63
- 779 Williams KD, Harris CM, Bodas-Salcedo A, Camp J, Comer RE, Copsey D, Fereday D, Gra-  
780 ham T, Hill R, Hinton T, Hyder P, Ineson S, Masato G, Milton SF, Roberts MJ, Rowell  
781 DP, Sanchez C, Shelly A, Sinha B, Walters DN, West A, Woollings T, Xavier PK (2015)  
782 The Met Office global coupled model 2.0 (GC2) configuration. *Geosci Model Dev Discuss*  
783 8:521–565
- 784 Wittenberg AT (2009) Are historical records sufficient to constrain ENSO simulations? *Geo-*  
785 *phys Res Lett* 36:L12,702
- 786 Xie SP, Philander SGH (1994) A coupled ocean-atmosphere model of relevance to the itcz in  
787 the eastern pacific. *Tellus* 46:340–350
- 788 Yu JY, Kao PK, Paek H, Hsu HH, Hung CW, Lu MM, An SI (2015) Linking emergence of  
789 the central Pacific El Niño to the Atlantic multidecadal oscillation. *J Clim* 28:651–662